C. R. Mecanique 347 (2019) 406–422

Contents lists available at ScienceDirect

Comptes Rendus Mecanique

www.sciencedirect.com

Thermohydrodynamic characteristics of combined double-diffusive radiation convection heat transfer in a cavity

Mohammad Foruzan Nia, Seyyed Abdolreza Gandjalikhan Nassab *

Mechanical Engineering Department, School of Engineering, Shahid Bahonar University of Kerman, Kerman, Iran

ARTICLE INFO

Article history:
Received 12 December 2018
Accepted 27 February 2019
Available online 18 March 2019

Keywords:
Double diffusive natural convection
Volumetric radiation
Cavity

ABSTRACT

This work deals with the numerical analysis of a radiating gas flow caused by both temperature and buoyancy concentration gradients in a square cavity; in this regard, the set of governing equations, including conservation of mass, momentum, species, and energy are solved by a numerical technique. In terms of radiation, since the fluid is considered as a semitransparent medium, the radiative term in the energy equation appears and is calculated by numerical solving of the radiative transfer equation (RTE). Furthermore, all of the surrounding cavity walls are considered to be opaque, gray, and diffuse with constant emissivity. All of the flow equations are solved by the finite difference method (FDM) and the RTE by the discrete ordinate one (DOM). In the present study, an attempt is made to verify the optical thickness effects on flow, thermal behavior, and mass transform in a cavity flow, such that reciprocating trends were seen in this manner. Our numerical results show that the thermal field in double-diffusive convection flow reaches very fast its steady-state situation in comparison to the concentration distribution. Besides, it is found that the thermohydrodynamic characteristics of a double-diffusive convection flow of a radiating gas are much affected by optical thickness.

1. Introduction

There are many industrial applications in which the phenomena of double-diffusive natural convection play a vital role. One can recall oceanography geophysics, petrology and crystal growth in material processing. The buoyancy forces due to simultaneous temperature and concentration gradients are driving factors in many types of convective flow. It is evident that in high-temperature systems, the radiative energy transfer becomes important beside the convective and conductive ones.

Many studies about combined convection radiation heat transfer in different geometries and in the absence of any concentration gradient have been released. Kumar and Eswaran [1] analyzed combined radiation and natural convection in a three-dimensional differentially heated rectangular cavity by the finite volume method. Their numerical results include a wide range of optical thickeners from 0 to 100, for a fixed Rayleigh number $Ra = 10^5$. As a noticeable finding, it was explained that the behavior of the temperature field is two dimensional, but the velocity field is three dimensional. Chang et al. [2] investigated combined radiation and natural convection in square enclosures with partitions mounted at the

---

* Corresponding author.
E-mail addresses: shmohammad4802@gmail.com (M. Foruzan Nia), Ganj110@k.ac.ir (S.A. Gandjalikhan Nassab).

https://doi.org/10.1016/j.crme.2019.02.003

Nomenclature

c	Concentration	$\mathrm{kg \cdot m^{-3}}$
C	Dimensionless concentration	
D	Diffusion coefficient	$\mathrm{m^2 \cdot s^{-1}}$
Df	Dufour coefficient	
g	Gravitational acceleration	$\mathrm{m \cdot s^{-2}}$
I	Radiation intensity	$\mathrm{W \cdot m^{-2}}$
I^*	Dimensionless radiation intensity	
I_b	Black body radiation intensity	$\mathrm{W \cdot m^{-2}}$
K_c	Dufour coefficient	$\mathrm{m^5\ K \cdot kg^{-1} \cdot s^{-1}}$
K_T	Soret coefficient	$\mathrm{kg \cdot m^{-1} \cdot K^{-1} \cdot s^{-1}}$
L	Width of cavity	m
Le	Lewis number	
N	Buoyancy ratio	
Nu	Nusselt number	
Pl	Plank number	
Pr	Prandtl number	
Q	Total heat transfer	
Ra	Rayleigh number	
Sh	Sherwood number	
Sr	Soret coefficient	
t	Time	s
t^*	Dimensionless time	
T	Temperature	K
(U, V)	Dimensionless horizontal and vertical velocity components	
(u, v)	Dimensional horizontal and vertical velocity components	$\mathrm{m \cdot s^{-1}}$
(X, Y)	Dimensionless horizontal and vertical coordinates, respectively	

Greek symbols

α	Thermal diffusivity	$\mathrm{m^2 \cdot s^{-1}}$
β_c	Solute volumetric expansion	$\mathrm{m^3 \cdot kg^{-1}}$
β_T	Coefficient of thermal expansion	$\mathrm{K^{-1}}$
ε	Emissivity coefficient	
ζ	Albedo coefficient	
θ	Dimensionless temperature	
ν	Kinematic viscosity	$\mathrm{m^2 \cdot s^{-1}}$
σ_s	Scattering coefficient	$\mathrm{m^{-1}}$
σ	Stefan–Boltzmann constant	$5.67 \times 10^{-8}\ \mathrm{W \cdot m^{-2} \cdot K^{-4}}$
σ_a	Absorption coefficient	$\mathrm{m^{-1}}$
τ	Optical thickness	
ϕ	Dimensionless temperature parameter	
ψ	Stream function	$\mathrm{m^2 \cdot s^{-1}}$
Ψ	Dimensionless stream function	
ω	Dimensionless vorticity	
Ω	Solid angle	

Subscripts

c	cold
h	hot
m	time step

midpoint of the ceiling and the floor in order to study the effects of both radiative gas and walls on the velocity and temperature fields and on the overall heat transfer. Webb and Viskanta [3] carried out a numerical study of the coupled heat transfer problem that involved both convection and radiation in a rectangular cavity. Lari et al. [4] analyzed the effect of radiative heat transfer on natural convection in a square cavity in standard room conditions. It was reported that neglecting the radiation effect in this combined heat transfer introduces considerable error in computing temperature distribution.

Recently, some authors published a paper in which the combined radiation and natural convection of a radiating gas inside a double-space cavity with conducting walls is numerically simulated [5]. The set of governing equations, including conservation of mass, momentum, and energy for the working fluid along with the RTE for radiation computation is solved by a numerical approach in transient conditions. The effect of optical thickness on the cooling rate of the system is thoroughly explored.

Regarding the process of double-diffusive natural convection in non-radiating media, there are also several papers in the literature. Teamah [6] presented a paper in which a double-diffusive convective flow in a rectangular cavity with upper and lower surfaces insulated and impermeable was investigated. On left and right walls, constant temperatures and concentrations were imposed, and a laminar flow was considered at steady-state conditions. Varol et al. [7] analyzed a steady-state natural convection in a right-angle triangular enclosure, with insulated vertical wall, while its inclined and bottom surfaces were differentially heated. Moreover, the set of governing equations was numerically solved by the finite difference method. A numerical study of the double-diffusive laminar free convection in a right-angle triangular solar collector was performed by Rahman et al. [8]. Governing equations in vorticity-stream function form were discretized by the finite element method. The effects of the buoyancy ratio, inclination angle and thermal Rayleigh number on the flow and the thermal behavior of the system were explored.

As far as the process of double-diffuse free convection in the presence of volumetric radiation is concerned, there are a few published papers. In this respect, Moufekkir et al. [9] analyzed the aforementioned combined heat transfer in a square enclosure with constant temperature and concentration at the vertical surfaces, whereas other walls were assumed to be impermeable and insulated. The governing flow equations were numerically solved by a hybrid technique employing the lattice Boltzmann method. In the gas energy equation, the radiative term was computed by a radiant intensity field inside the participating medium via the radiative transfer equation. Also, this equation was solved by the well-known discrete ordinates method. Numerical results were presented by plotting the streamlines and isotherm lines under a fixed optical thickness. Besides, the influence of the buoyancy number and of the boundary wall emissivity on the flow field and mass transfer were completely examined.

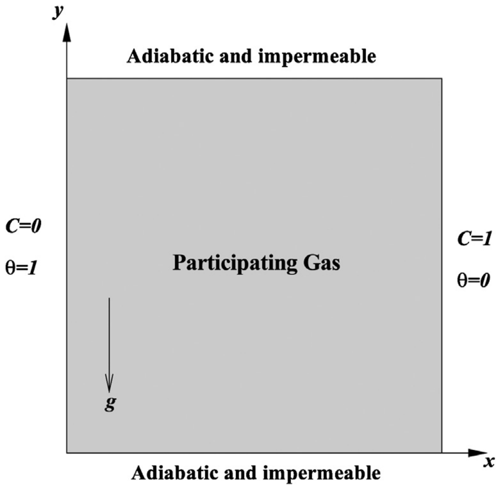

Fig. 1. Scheme of the thermal system.

Although there are a few works about the double-diffuse free convection combined with volumetric radiation, the radiative properties effects of the participating medium such as optical thickness were not analyzed clearly in transient conditions. This motivated the authors to numerically investigate the radiative thermal behavior of double-diffusive convection in a square cavity.

The set of flow equations in vorticity-stream function forms are considered and numerically solved by the finite difference method, while the solution to the RTE is obtained by DOM. Also, so as to find the thermohydrodynamic characteristics of the thermal system in the transient period of its working, the governing equations are considered in unsteady forms. The main goal is to verify the effect of optical thickness on the performance of the thermal system in the transient time period of the thermal system.

2. Mathematical formulation

The schematic of system considered in this study is shown in Fig. 1. The cavity is filled with a binary participating gas that behaves as a Newtonian, incompressible, and gray medium. On the horizontal boundary surfaces, insulated and impermeable conditions are assumed, whereas different temperatures (T_h, T_c) and concentrations (C_c, C_h) are imposed on the left and right walls, respectively. All thermophysical properties of the semitransparent gas are assumed constant, except density, which is varied according to the Boussinesq approximation. The driving forces for introducing the gas flow are the buoyancies due to temperature and concentration gradients.

Two different factors for generating the convective flow are the temperature gradient and the concentration gradient, which lead to heat and mass buoyancy forces, respectively. These forces may be in the same direction or in the opposite sense regarding the boundary conditions.

The density of the mixture is computed from the reference state as a base line ($c = c_0$, $T = T_0$, $\rho = \rho_0$) as follows [10]:

$$\rho = \rho_0 [1 - \beta_T (T - T_0) - \beta_\text{c} (c - c_0)]$$

where β_T and β_c are the thermal and solatal volumetric expansion, respectively. Their values can be found using the following relations.

$$\beta_T = \frac{-1}{\rho_0}\left(\frac{\partial \rho}{\partial T}\right)_C \quad \text{and} \quad \beta_\text{c} = \frac{-1}{\rho_0}\left(\frac{\partial \rho}{\partial C}\right)_T$$

The governing differential equations for transient, incompressible, laminar buoyancy convection and constant property flow with Soret and Dufour effects are non-dimensionalized by the following parameters:

$$X = \frac{x}{L}, \quad Y = \frac{y}{L}, \quad U = \frac{u\,L}{\alpha}, \quad V = \frac{v\,L}{\alpha}, \quad \theta = \frac{T - T_\text{c}}{T_\text{h} - T_\text{c}}, \quad C = \frac{c - c_\text{c}}{c_\text{h} - c_\text{c}}, \quad Pr = \frac{\nu}{\alpha} \tag{1}$$

$$N = \frac{\beta_\text{c}(c_\text{h} - c_\text{c})}{\beta_T (T_\text{h} - T_\text{c})}, \quad Le = \frac{\alpha}{D}, \quad Sr = \frac{k_T (c_\text{h} - c_\text{c})}{\alpha (T_\text{h} - T_\text{c})}, \quad Df = \frac{k_\text{c}(T_\text{h} - T_\text{c})}{\alpha (c_\text{h} - c_\text{c})} \quad Ra = \frac{g L^3 \beta_T (T_\text{h} - T_\text{c})}{\nu \alpha}$$

Vorticity equation:

$$\frac{\partial \omega}{\partial t^*} + U \frac{\partial \omega}{\partial X} + V \frac{\partial \omega}{\partial Y} = Pr \left(\frac{\partial^2 \omega}{\partial X^2} + \frac{\partial^2 \omega}{\partial Y^2}\right) + Ra \cdot Pr \left(\frac{\partial \theta}{\partial X} + N \frac{\partial C}{\partial X}\right) \tag{2}$$

where

$$\omega = -\left(\frac{\partial^2 \Psi}{\partial X^2} + \frac{\partial^2 \Psi}{\partial Y^2}\right) \tag{3}$$

Mass equation:

$$\frac{\partial C}{\partial t^*} + U\frac{\partial C}{\partial X} + V\frac{\partial C}{\partial Y} = \frac{1}{Le}\left[\left(\frac{\partial^2 C}{\partial X^2} + \frac{\partial^2 C}{\partial Y^2}\right) + Sr\left(\frac{\partial^2 \theta}{\partial X^2} + \frac{\partial^2 \theta}{\partial Y^2}\right)\right] \tag{4}$$

Energy equation:

$$\frac{\partial \theta}{\partial t^*} + U\frac{\partial \theta}{\partial X} + V\frac{\partial \theta}{\partial Y} = \left(\frac{\partial^2 \theta}{\partial X^2} + \frac{\partial^2 \theta}{\partial Y^2}\right) + Df\left(\frac{\partial^2 C}{\partial X^2} + \frac{\partial^2 C}{\partial Y^2}\right) - \frac{1}{Pl\cdot\varphi}\nabla^*\cdot Q \tag{5}$$

$\nabla^*\cdot Q$ represents the divergence of the radiative heat flux, which has appeared as a source term in the energy equation of the participating gases. It can be calculated as follows [11]:

$$\nabla^*\cdot Q = \tau(1-\zeta)\cdot\left[4(\theta\phi+1)^4 - \int_{4\pi} I^*\mathrm{d}\Omega\right] \tag{6}$$

in which τ is the optical thickness, ζ is the albedo coefficient, ϕ is the dimensionless temperature parameter, and I^* is a non-dimensional form of the radiation intensity. The radiant intensity inside the participating medium is obtained from the radiative transfer equation as follows [11]:

$$\frac{1}{\tau}(\Omega\cdot\nabla)I^* = \frac{1-\zeta}{\pi}(\theta_{\mathrm{f}}\phi+1)^4 - I^* + \frac{\zeta}{4\pi}\int_{4\pi} I^*\mathrm{d}\Omega' \tag{7}$$

To summarize the paper, the numerical solution to the RTE by DOM, which was explained in the previous study by the authors [12], is not explained here.

2.1. Boundary and initial conditions in the non-dimensional forms

The following boundary condition is applied to solve the RTE:

$$I^* = \varepsilon_{\mathrm{w}} I_{\mathrm{b}}{}^* + \frac{(1-\varepsilon_{\mathrm{w}})}{\pi}\int_{\vec{n}_{\mathrm{w}}\cdot\vec{s}'<0} I^*\left|\vec{n}_{\mathrm{w}}\cdot\vec{s}'\right|\mathrm{d}\Omega' \qquad \vec{n}_{\mathrm{w}}\cdot\vec{s} > 0 \tag{8}$$

In the numerical solution to the flow equations, a no-slip boundary condition is considered at the solid boundaries, so the boundary and initial conditions can be written as follows:

$$Y = 0 \quad \frac{\partial\psi}{\partial X} = \frac{\partial\psi}{\partial Y} = Q = \frac{\partial C}{\partial Y} = 0 \tag{9}$$

$$Y = 1 \quad \frac{\partial\psi}{\partial X} = \frac{\partial\psi}{\partial Y} = Q = \frac{\partial C}{\partial Y} = 0 \tag{10}$$

$$X = 0 \quad \frac{\partial\psi}{\partial X} = \frac{\partial\psi}{\partial Y} = 0,\ \theta = 1,\ \ C = 0 \tag{11}$$

$$X = 1 \quad \frac{\partial\psi}{\partial X} = \frac{\partial\psi}{\partial Y} = 0,\ \theta = 0,\ \ C = 1 \tag{12}$$

$$t^* = 0 \quad \frac{\partial\psi}{\partial X} = \frac{\partial\psi}{\partial Y} = 0,\ \theta = 0,\ \ C = 0 \tag{13}$$

3. The main physical quantities

According to the double-diffusive natural convection due to both temperature and concentration gradients, the rates of heat and mass transfer through the cavity can be characterized by the overall Nusselt and Sherwood numbers as follows [5,9]:

$$Nu_{\mathrm{ove}} = \left.\frac{\partial\theta}{\partial X}\right|_{X=0} + Df\left.\frac{\partial C}{\partial X}\right|_{X=0} - \frac{1}{Pl\,\phi}\left((1+\phi\,\theta)^4 - \sum_{n\cdot s_{\mathrm{w}}} I^*\left|\vec{n}_{\mathrm{w}}\cdot\vec{s}'\right|\Omega_i\right) \tag{14}$$

$$Sh = \left.\frac{\partial C}{\partial X}\right|_{X=0} + Sr \left.\frac{\partial \theta}{\partial X}\right|_{X=0} \tag{15}$$

where the first, second, and third terms in Eq. (14) indicate the Fourier heat flux due to conduction, the diffusion thermo-flux owing to the Dufour effect and the radiative flux, respectively. Moreover, in Eq. (15), the first and second terms represent the Dufour and Fourier parts of mass transfer.

4. Numerical procedure

The finite difference method is used for discretizing the vorticity, energy, and mass equations, while the time linearization technique is employed to compute nonlinear terms. The values of vorticity at time steps $m+1$ and $m+2$ based on the ADI technique can be obtained as follows [13,14]:

$$\frac{\partial \omega}{\partial t^*} + \left(U\frac{\partial \omega}{\partial X}\right)_{m+1} + \left(V\frac{\partial \omega}{\partial Y}\right)_{m} = Pr\left(\left(\frac{\partial^2 \omega}{\partial X^2}\right)_{m+1} + \left(\frac{\partial^2 \omega}{\partial Y^2}\right)_{m}\right) + Ra{\cdot}Pr\left(\frac{\partial \theta}{\partial X}\right)_{m} \tag{16}$$

$$\frac{\partial \omega}{\partial t^*} + \left(U\frac{\partial \omega}{\partial X}\right)_{m+1} + \left(V\frac{\partial \omega}{\partial Y}\right)_{m+2} = Pr\left(\left(\frac{\partial^2 \omega}{\partial X^2}\right)_{m+1} + \left(\frac{\partial^2 \omega}{\partial Y^2}\right)_{m+2}\right) + Ra{\cdot}Pr\left(\frac{\partial \theta}{\partial X}\right)_{m+1} \tag{17}$$

where the stream function at time steps $m+1$ and $m+2$ is calculated by Eq. (18) and Eq. (19):

$$\omega_{m+1} = -\left(\frac{\partial^2 \Psi}{\partial X^2} + \frac{\partial^2 \Psi}{\partial Y^2}\right)_{m+1} \tag{18}$$

$$\omega_{m+2} = -\left(\frac{\partial^2 \Psi}{\partial X^2} + \frac{\partial^2 \Psi}{\partial Y^2}\right)_{m+2} \tag{19}$$

Based on the numerical technique, for calculating the gas temperature at time steps $m+1$ and $m+2$, the following equations are used:

$$\begin{aligned}&\left(\frac{\partial \theta}{\partial t^*}\right) + \left(U\frac{\partial \theta}{\partial X}\right)_{m+1} + \left(V\frac{\partial \theta}{\partial Y}\right)_{m} = \left(\frac{\partial^2 \theta}{\partial X^2}\right)_{m+1} + \left(\frac{\partial^2 \theta}{\partial Y^2}\right)_{m} + \\ &Df\left(\frac{\partial^2 C}{\partial X^2} + \frac{\partial^2 C}{\partial Y^2}\right)_{m} - \frac{\tau(1-\zeta)}{Pl{\cdot}\phi}\left(4\,(\theta\,\phi+1)^4 - \sum_{i=1}^{n'} I_i^* w_i\right)_{m}\end{aligned} \tag{20}$$

$$\begin{aligned}&\left(\frac{\partial \theta}{\partial t^*}\right) + \left(U\frac{\partial \theta}{\partial X}\right)_{m+1} + \left(V\frac{\partial \theta}{\partial Y}\right)_{m+2} = \left(\frac{\partial^2 \theta}{\partial X^2}\right)_{m+1} + \left(\frac{\partial^2 \theta}{\partial Y^2}\right)_{m+2} + \\ &Df\left(\frac{\partial^2 C}{\partial X^2} + \frac{\partial^2 C}{\partial Y^2}\right)_{m+1} - \frac{\tau\,(1-\zeta)}{Pl{\cdot}\phi}\left(4\,(\theta\,\phi+1)^4 - \sum_{i=1}^{n'} I_i^* w_i\right)_{m+1}\end{aligned} \tag{21}$$

In the calculation of concentration, a similar method is used, and the linearization forms of the mass equation along with the ADI technique become:

$$\left(\frac{\partial C}{\partial t^*}\right) + \left(U\frac{\partial C}{\partial X}\right)_{m+1} + \left(V\frac{\partial C}{\partial Y}\right)_{m} = \frac{1}{Le}\left[\left(\frac{\partial^2 C}{\partial X^2}\right)_{m+1} + \left(\frac{\partial^2 C}{\partial Y^2}\right)_{m} + Sr\left(\frac{\partial^2 \theta}{\partial X^2} + \frac{\partial^2 \theta}{\partial Y^2}\right)_{m}\right] \tag{22}$$

$$\left(\frac{\partial C}{\partial t^*}\right) + \left(U\frac{\partial C}{\partial X}\right)_{m+1} + \left(V\frac{\partial C}{\partial Y}\right)_{m+2} = \frac{1}{Le}\left[\left(\frac{\partial^2 C}{\partial X^2}\right)_{m+1} + \left(\frac{\partial^2 C}{\partial Y^2}\right)_{m+2} + Sr\left(\frac{\partial^2 \theta}{\partial X^2} + \frac{\partial^2 \theta}{\partial Y^2}\right)_{m+1}\right] \tag{23}$$

The discretized forms of equations (16) to (23) are solved by a line-by-line procedure, along with the tridiagonal matrix algorithm (TDMA) and the successive over-relaxation (SOR) technique.

So as to estimate the derivative terms in the non-uniform grid (Fig. 2), the following relations are employed [15]:

$$\left.f_x\right|_{i,j} = \frac{1}{\Delta x_- \Delta x_+^2 + \Delta x_+ \Delta x_-^2}\left[\Delta x_-^2 f_{i+1,j} + (\Delta x_+^2 - \Delta x_-^2) f_{i,j} - \Delta x_+^2 f_{i-1,j}\right] \tag{24}$$

$$\left.f_y\right|_{i,j} = \frac{1}{\Delta y_- \Delta y_+^2 + \Delta y_+ \Delta y_-^2}\left[\Delta y_-^2 f_{i,j+1} + (\Delta y_+^2 - \Delta y_-^2) f_{i,j} - \Delta y_+^2 f_{i,j-1}\right] \tag{25}$$

$$\left.f_{xx}\right|_{i,j} = \frac{2}{\Delta x_- \Delta x_+^2 + \Delta x_+ \Delta x_-^2}\left[\Delta x_- f_{i+1,j} - (\Delta x_+ + \Delta x_-) f_{i,j} + \Delta x_+ f_{i-1,j}\right] \tag{26}$$

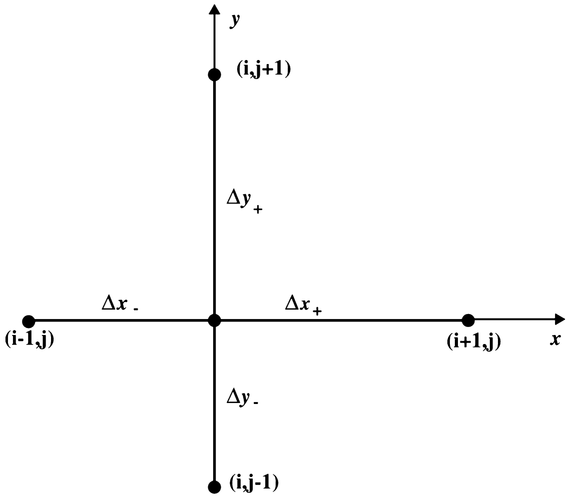

Fig. 2. Discretized computational non-uniform grid.

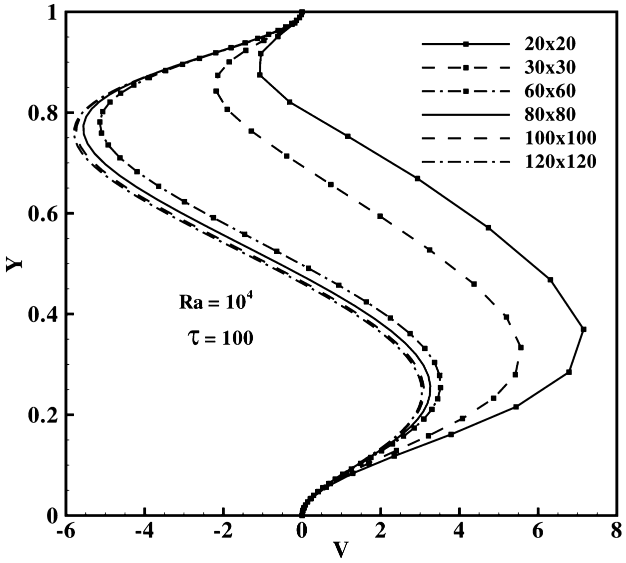

Fig. 3. Grid study in the calculation of the V-velocity component inside the cavity.

$$f_{yy}\Big|_{i,j} = \frac{2}{\Delta y_- \Delta y_+^2 + \Delta y_+ \Delta y_-^2}\left[\Delta y_- f_{i,j+1} - (\Delta y_+ + \Delta y_-) f_{i,j} + \Delta y_+ f_{i,j-1}\right] \tag{27}$$

where f can be one of the dependent variables, namely, ω, Ψ, θ, and C.

The numerical procedure can be summarized as follows:

1) initialize all of the dependent variables;
2) the mentioned discretized continuity, vorticity and energy equations are solved;
3) the RTE is solved by DOM for computation of radiant intensity at each time level;
4) the radiative term (divergence of radiative heat flux) in the gas energy equation is computed;
5) steps 2 to 4 are repeated until the aforementioned equations converge;
6) initialize new time step and dependent variables;
7) steps 2 to 6 are repeated until the steady state achieves.

Numerical calculations were carried out by writing a computer program in FORTRAN. It should be mentioned that, to compute the divergence of the radiative heat flux, which is needed for the numerical resolution of the energy equation by DOM, a S_6 approximation, which represents the numbers of directions being used for discretizing the RTE, has been used in this study (S_N denotes to $N(N+1)$ discrete directions). Numerical solutions are iteratively obtained such that iterations are

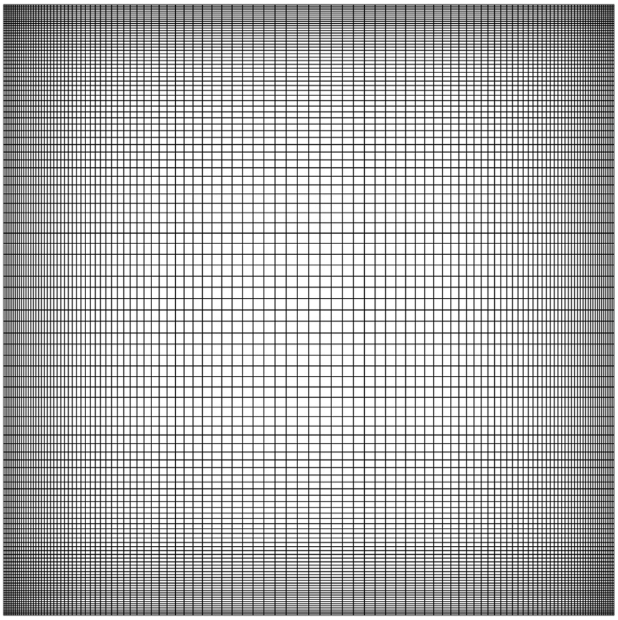

Fig. 4. Discretized computational domain with non-uniform grids.

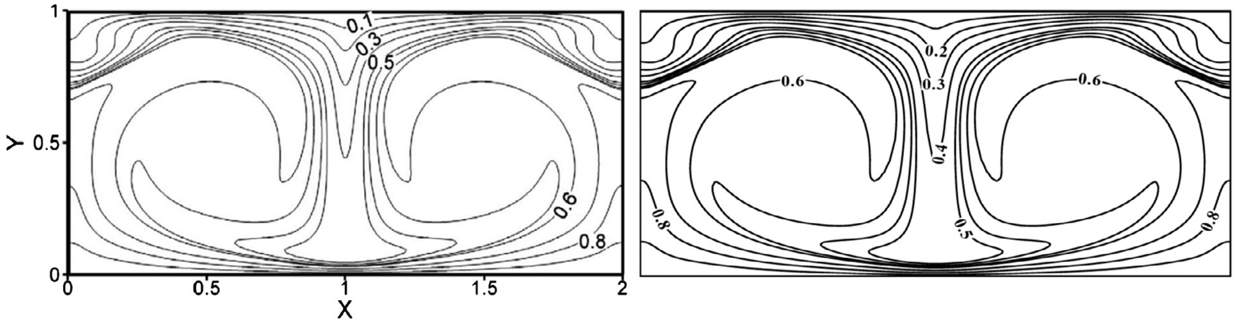

(a) Wang et al. [10]

(b) Present study

Fig. 5. Distributions of the isotherm lines $N = 5.0$, $Ra = 10^5$, $Le = 2$, and $Sr = Df = 0.1$.

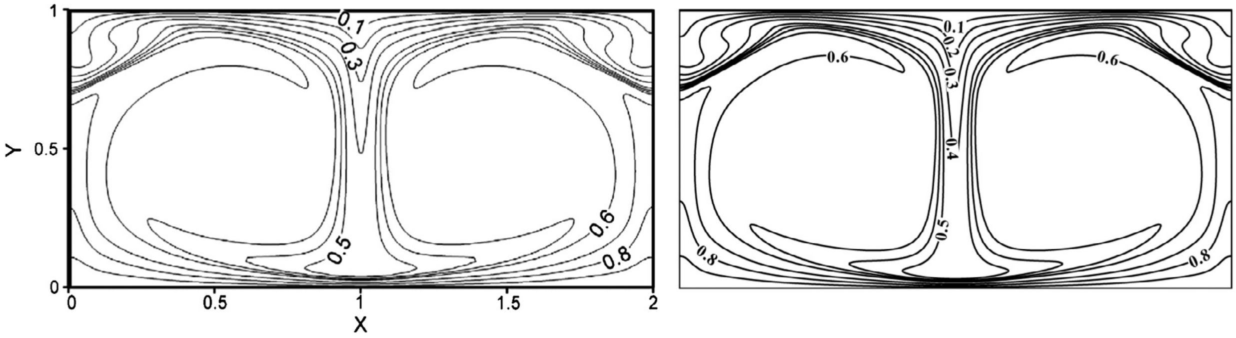

(a) Wang et al. [10]

(b) Present study

Fig. 6. Distributions of the iso-concentration lines $N = 5.0$, $Ra = 10^5$, $Le = 2$, and $Sr = Df = 0.1$.

ended when the sum of the absolute residuals is less than 10^{-6} for vorticity, mass, and energy equations at each time step. Moreover, in the numerical solution to the RTE, the maximum difference between the radiative intensities calculated during two consecutive iteration levels did not exceed 10^{-7} at each nodal point for the converged solution. It is worth to mention that the numerical results for each dependent variables reach their steady values by marching in time with the optimum time step.

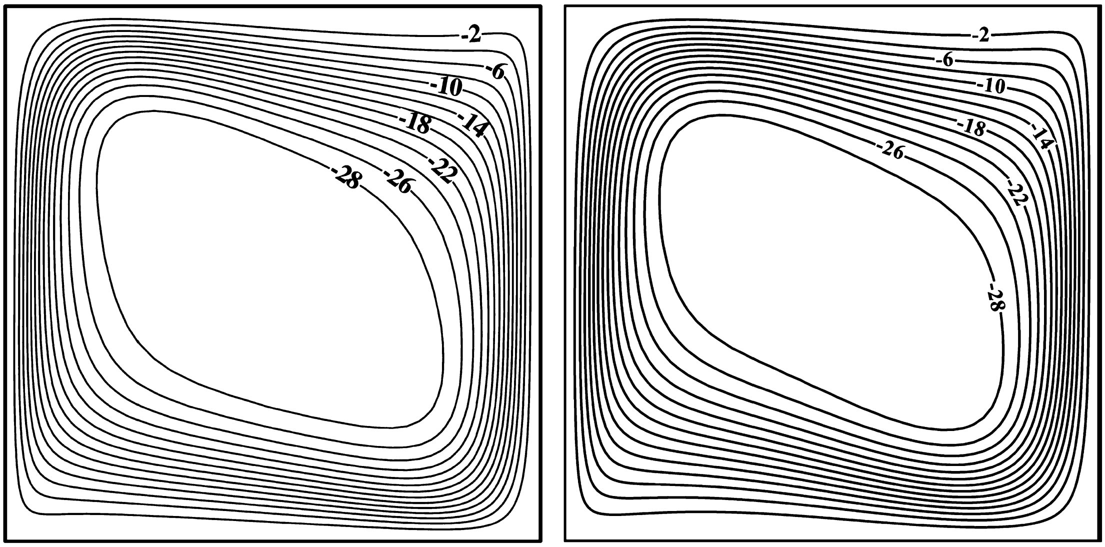

(a) Lari et al. [4] (b) Present study

Fig. 7. Distribution of the streamlines.

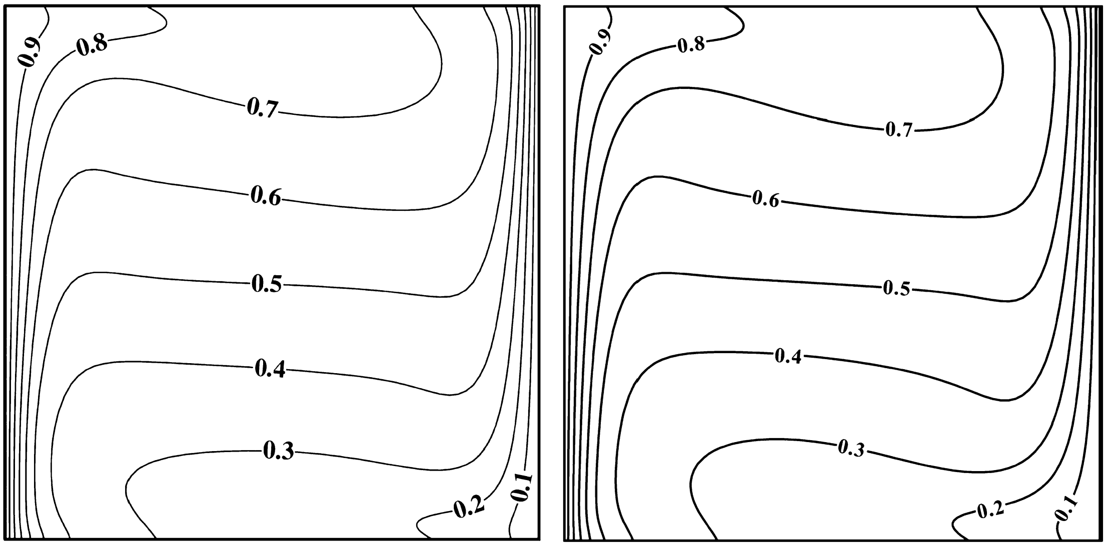

(a) Lari et al. [4] (b) Present study

Fig. 8. Distribution of the isotherm lines.

5. Grid refinement

So as to find the grid-independent numerical solution, numerous attempts at choosing the parameter that is more sensitive by grid size have been done. Consequently, the velocity components with high values of optical thicknesses have this feature. In this regard, the distributions of the V-velocity component of the buoyant gas flow at the vertical mid-plane of the cavity with optical thickness $\tau = 100$ are calculated using different mesh sizes, as shown in Fig. 3. Based on the findings depicted in Fig. 3, the grid size of 100×100 is determined as the optimum one and will be used in subsequent calculations. It should be mentioned that the grid size for all of the governing equations, which are velocity, temperature, concentration, and also the radiant intensity, is the same, but with clustering near the solid walls for higher accuracy. The schematic of the discretized computational domain is shown in Fig. 4. Since the governing equations are solved in transient conditions, a time interval $\Delta t^* = 10^{-6}$ is used in the time marching process up to steady-state conditions.

Table 1
Values of the non-dimensional parameters [5,9].

Parameter	Pl	Pr	ϕ	ζ	Le	Sr	Df	N	ε
Value	0.1	0.7	$\frac{20}{300}$	0.5	1.641	0.1	0.1	−2	0.8

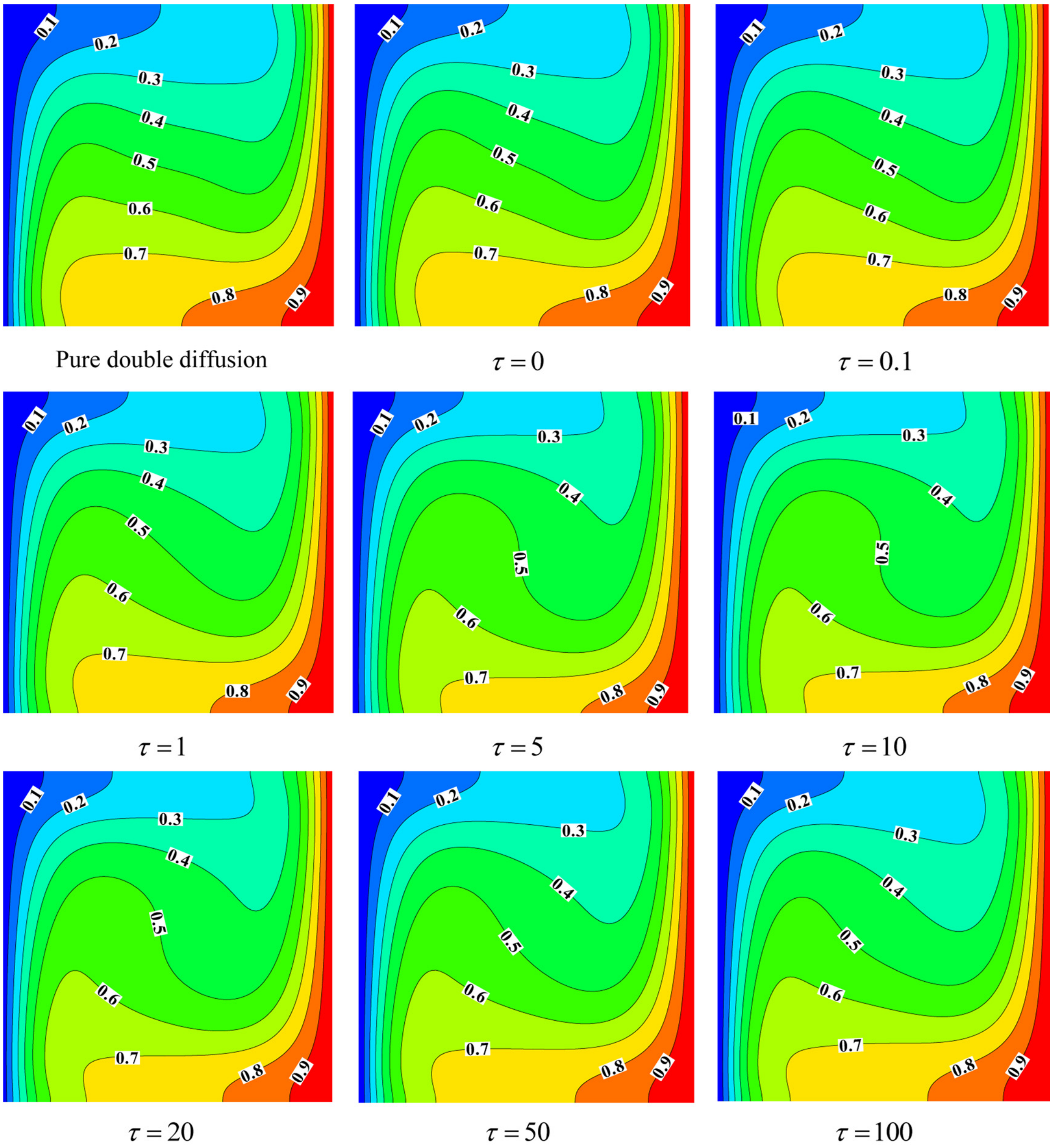

Pure double diffusion $\tau = 0$ $\tau = 0.1$

$\tau = 1$ $\tau = 5$ $\tau = 10$

$\tau = 20$ $\tau = 50$ $\tau = 100$

Fig. 9. Iso-concentration lines for $Ra = 10^4$ for different optical thicknesses in steady-state conditions.

6. Validation

6.1. Double diffuse case

To validate the numerical scheme in solving the set of governing equations, a double-diffusive convection flow inside a rectangular cavity with adiabatic vertical walls is simulated, while the bottom and top walls are isotherm, with hot and cold temperatures. Moreover, a concentration gradient governs the entire convective flow because of the difference between the species concentrations on the bottom and top walls. The plots of isotherm and iso-concentration lines are displayed in Fig. 5 and Fig. 6. The numerical results reported by Wang et al. [10] are also shown in this figure. By comparing, a good

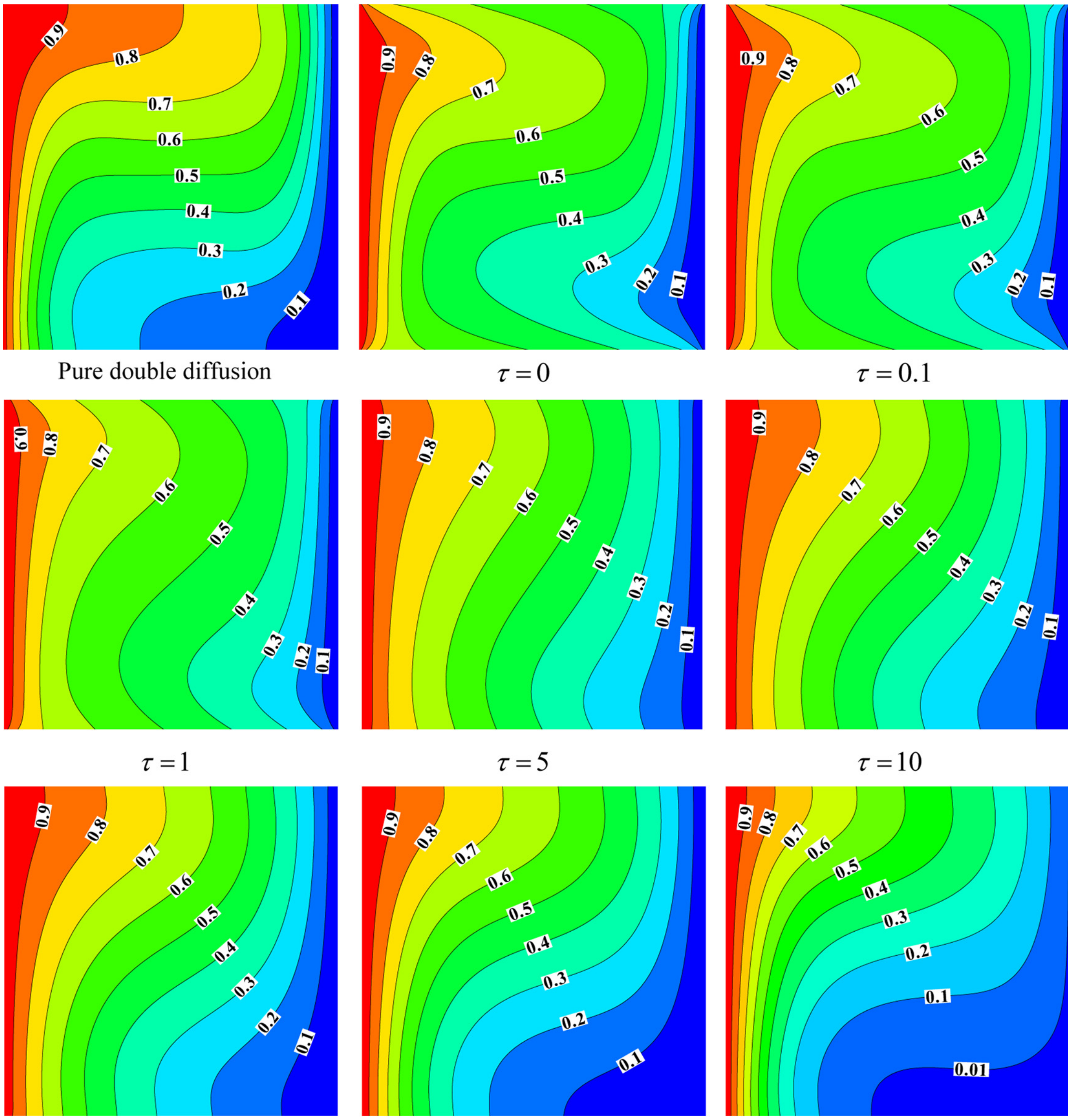

Pure double diffusion $\tau = 0$ $\tau = 0.1$

$\tau = 1$ $\tau = 5$ $\tau = 10$

$\tau = 20$ $\tau = 50$ $\tau = 100$

Fig. 10. Isotherm lines for $Ra = 10^4$ for different optical thicknesses in steady-state conditions.

consistency can be seen between the present numerical results and the theoretical findings of Wang et al. [10]. It is worth mentioning that, in the present test case, the flowing gas is assumed to be transparent in thermal radiation.

6.2. Combined radiation and natural convection case

To verify the radiative calculations in solving the RTE, a buoyant flow of radiating gas inside a cavity is simulated in the next test case, and the results are depicted in Fig. 7 and Fig. 8. In this test case, which was analyzed previously by the second author, a natural convection of gas flow in a cubic cavity with the hot right, cold left, and adiabatic top and bottom surfaces is considered. Fig. 7 shows a main recirculated flow inside the cavity because of the buoyant forces. In Fig. 8, the isotherm plots are demonstrated. It shows high temperature gradients along the horizontal sense, especially close to the hot and cold surfaces and uniformity in vertical direction. One should recall the fact that the isotherms are not perpendicular to the adiabatic walls owing to the existence of radiative heat transfer inside the gas flow in addition to the convective one. However, Fig. 7 and Fig. 8 show good consistencies between the present numerical analysis and the theoretical findings in Ref. [4].

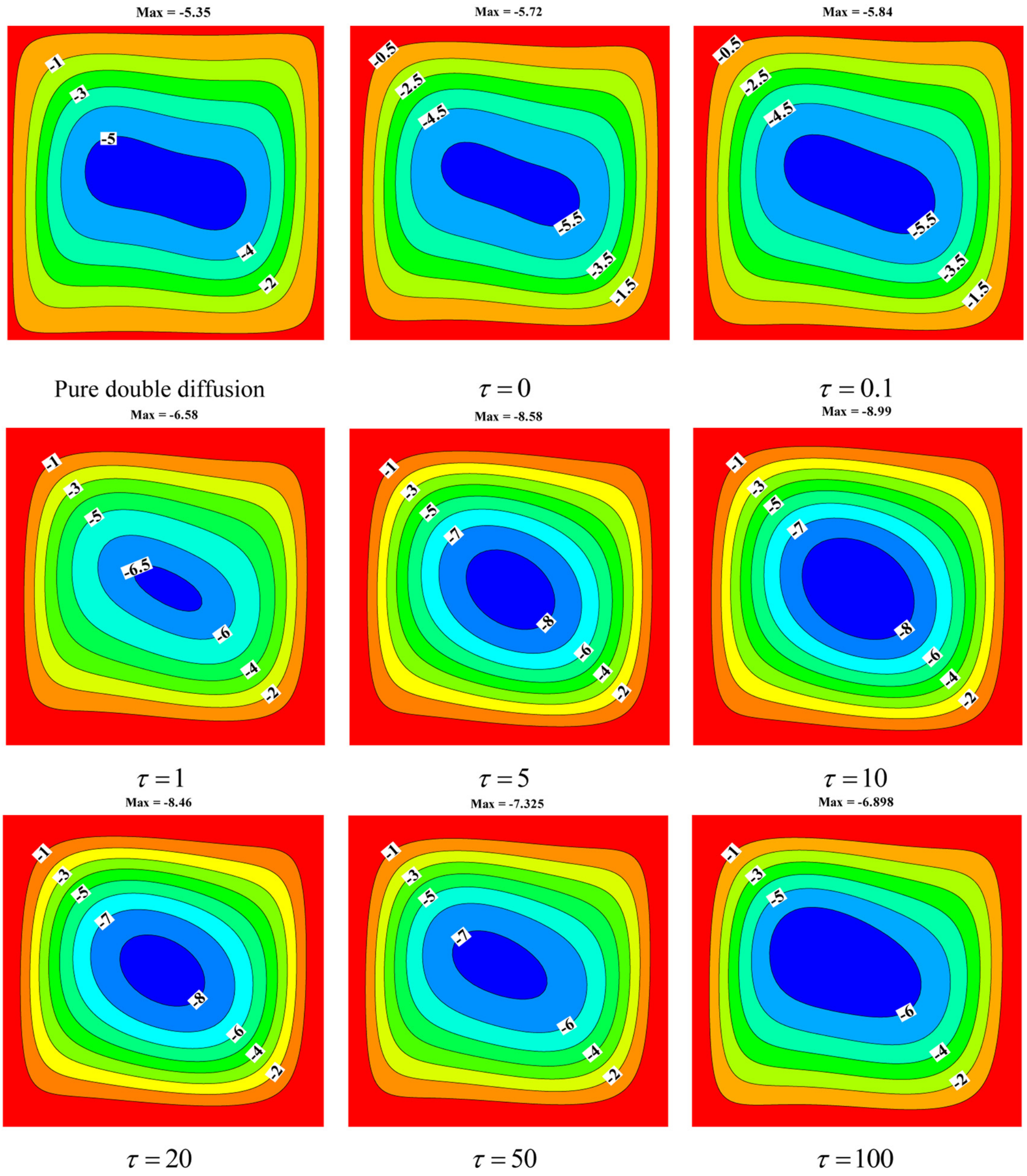

Pure double diffusion $\tau = 0$ $\tau = 0.1$

$\tau = 1$ $\tau = 5$ $\tau = 10$

$\tau = 20$ $\tau = 50$ $\tau = 100$

Fig. 11. Steady-state streamline distributions for $Ra = 10^4$ for different values of optical thickness.

7. Results

In this paper, an attempt is made to investigate the effect of volumetric radiation and of its properties on the thermo-hydrodynamic characteristics in the double-diffusive free convection of a semitransparent gas inside a cavity in transient conditions. The set of governing equations is solved by numerical techniques to obtain the velocity, temperature and concentration distributions inside the computational domain. The numerical results are presented by plotting the streamline, isotherm and iso-concentration lines in the cavity. In calculations of all subsequent results, the values of non-dimensional parameters, which have appeared in the governing equations, are the same as those given in Table 1. The values of the other non-dimensional parameters such as the Rayleigh number and optical thickness are mentioned for each case, individually. First, the concentration and temperature distributors for different values of the optical thickness ($\tau = 0$–100) in the enclosure at steady-state conditions are shown in Fig. 9 and Fig. 10 for $Ra = 10^4$. It should be noted that zero optical thickness denotes only surface radiation, whereas in the case of pure double-diffusion the surface radiation is also emitted. As these figures show, high gradients of temperature and concentration take place close to the left and right surfaces and

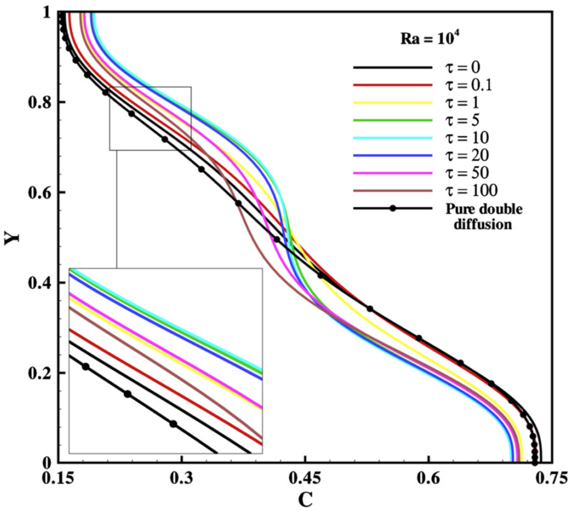

Fig. 12. Distribution of concentration along the vertical mid-line of the cavity for $Ra = 10^4$ at steady-state conditions.

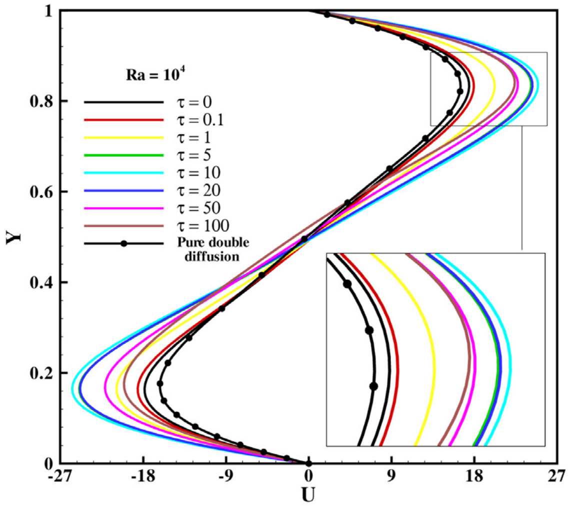

(a) U-Velocity

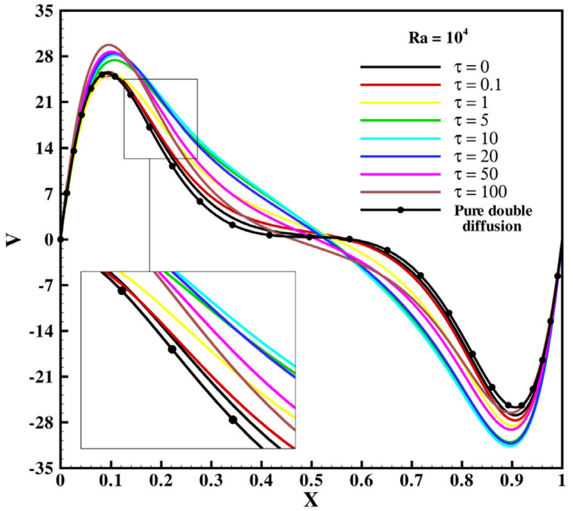

(b) V-Velocity

Fig. 13. Velocity distributions inside the cavity for $Ra = 10^4$ at steady-state conditions.

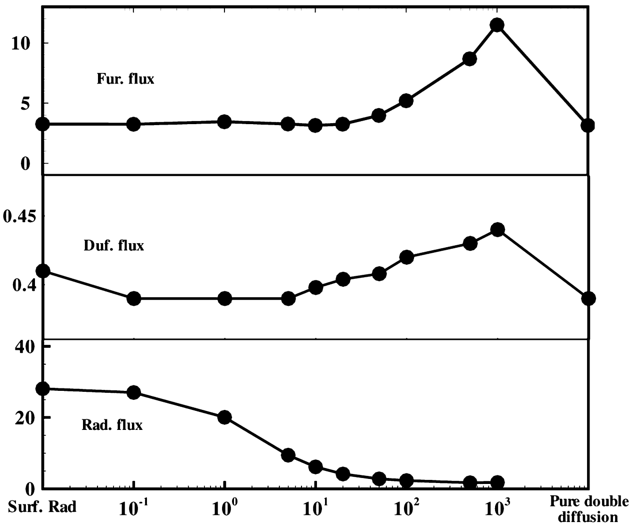

Fig. 14. Variations of the Fourier, Dufour, and radiative fluxes with optical thickness for $Ra = 10^4$ at steady-state conditions.

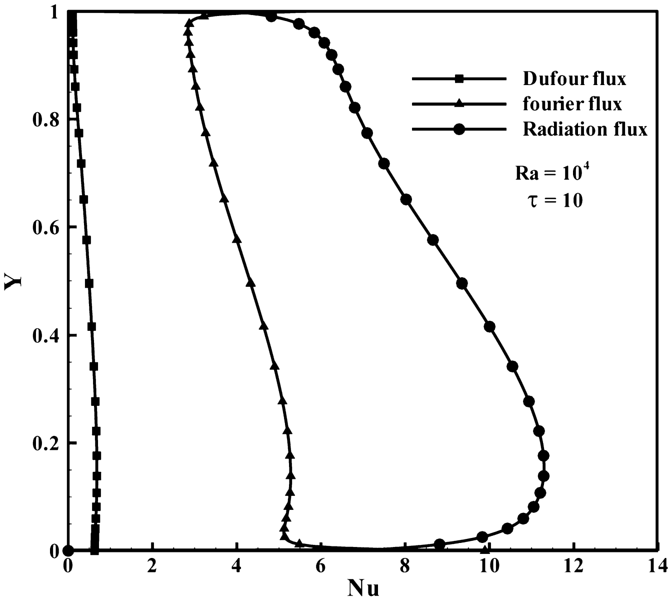

Fig. 15. Distributions of the Dufour, Fourier, and radiation Nusselt numbers.

low gradients close to the cavity center. Owing to impermeable bottom and top walls, the iso-concentration lines are perpendicular to these surfaces, while for isotherm lines, a small derivation from the right angle is seen adjacent to insulated surfaces due to the existence of radiation heat transfer in addition to its convection counterpart. Fig. 9 shows that optical thickness does not have considerable effect on the distribution of the concentration inside the cavity. Ironically, it is seen that the temperature field inside the cavity is much affected by the variation of optical thickness along sweep behavior.

In order to show the flow pattern, the streamline plots for different values of τ are plotted in Fig. 11. In all cases, there is a main recirculated zone at the center of cavity, which occupies the entire region of the enclosure and four small recirculated domains near the cavity corners (which are not shown). Fig. 11 shows how the buoyant gas flow is affected by the ability of radiation heat transfer as the optical thickness increases. The minimum rate of flow vortices takes place for pure double-diffusion. To clarify, it increases with increasing in optical thickness up to a certain value, and then a reverse trend is seen. Consequently, a reciprocating behavior for the gas flow with increasing optical thickness is seen in Fig. 11 as it was seen before in the previous figures. It should be noted that this behavior was also reported by Lari et al. [4] and was discussed in detail there. Indeed, when the optical thickness becomes very large, all of the radiation intensities are absorbed near the walls and cannot penetrate into the cavity. Therefore, the cavity with large optical thickness ($\tau = 100$) is like the one without radiation heat transfer (i.e. pure double-diffusion convective flow).

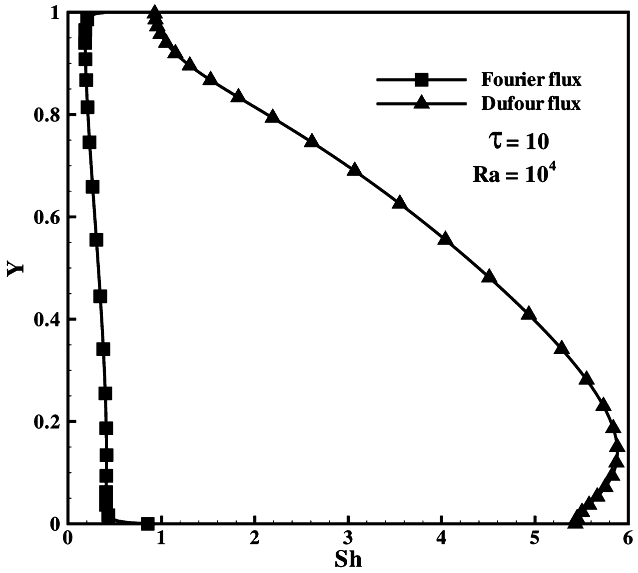

Fig. 16. Distributions of Dufour and Fourier Sherwood numbers.

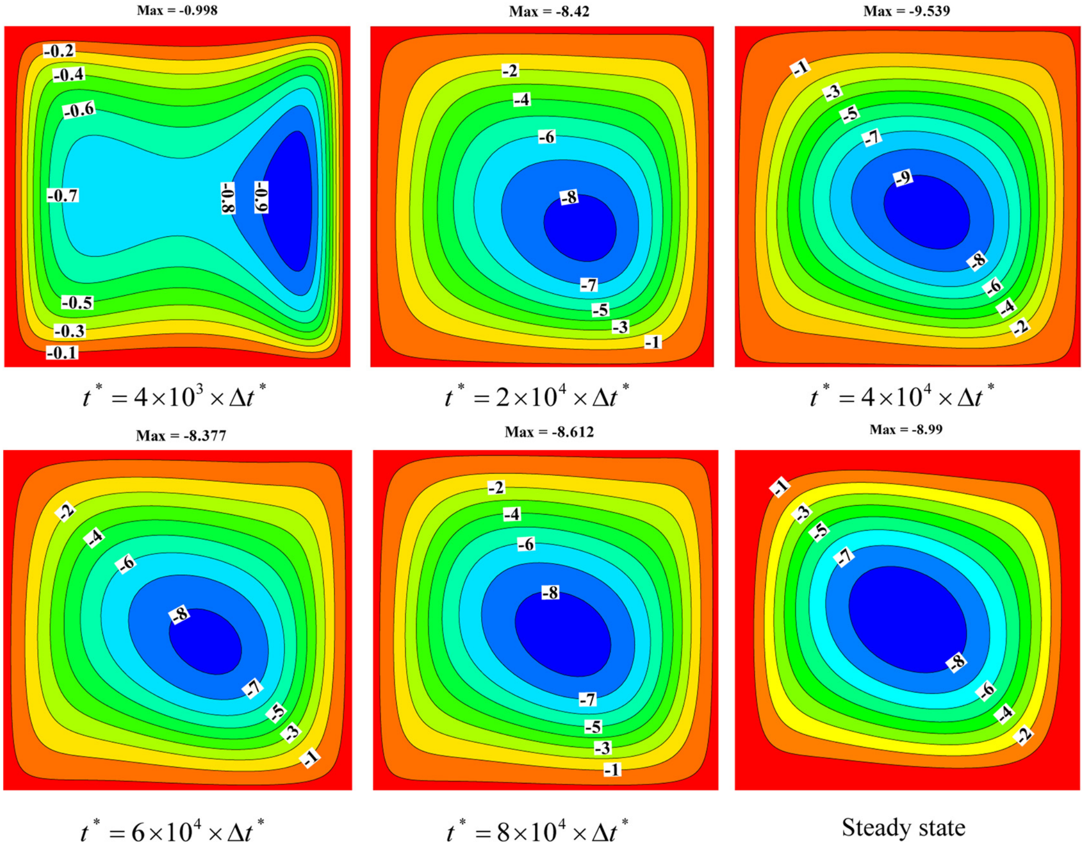

$t^* = 4\times10^3\times\Delta t^*$ $t^* = 2\times10^4\times\Delta t^*$ $t^* = 4\times10^4\times\Delta t^*$

$t^* = 6\times10^4\times\Delta t^*$ $t^* = 8\times10^4\times\Delta t^*$ Steady state

Fig. 17. Streamline for $Ra = 10^4$ at different time levels, $\tau = 10$.

To have a more clear figure for depicting the variation of concentration inside the enclosure, the distribution of concentration along the y-axis at the mid-plane of the cavity is shown in Fig. 12. This figure shows almost a linear trend for concentration with a small deviation by wavy forms. This figure also shows reciprocal behavior for concentration with increasing τ from surface radiation ($\tau = 0$) toward thick medium ($\tau = 100$).

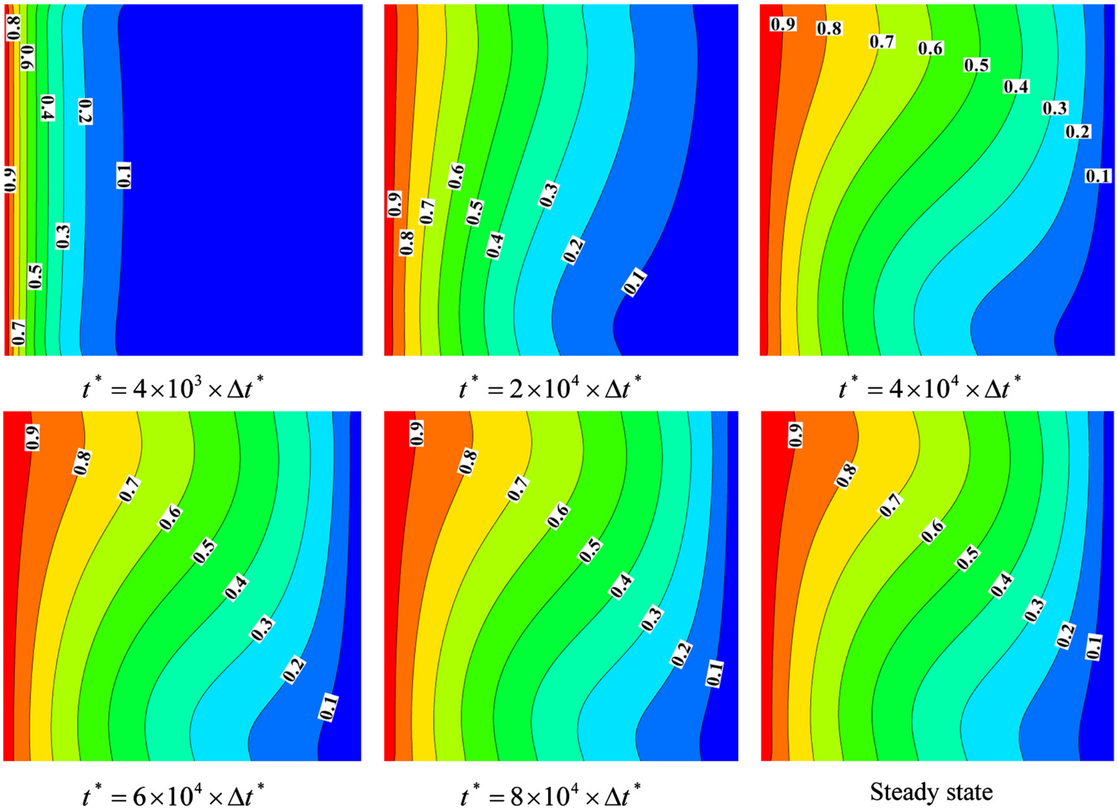

$t^* = 4 \times 10^3 \times \Delta t^*$ $t^* = 2 \times 10^4 \times \Delta t^*$ $t^* = 4 \times 10^4 \times \Delta t^*$

$t^* = 6 \times 10^4 \times \Delta t^*$ $t^* = 8 \times 10^4 \times \Delta t^*$ Steady state

Fig. 18. Isothermal lines for $Ra = 10^4$ at different time levels, $\tau = 10$.

The U and V-Velocity distributions at the mid-lines of the cavity are drawn in Fig. 13. This figure shows the upward gas flow near the hot surface and the downward one close to the cold one. This figure also reveals that the gas flow is affected by optical thickness, the lowest gas velocity is for the pure double-diffusion case and again a reciprocal trend is seen. To elaborate, by ascending optical thickness from 0 to 10, the velocity components increase especially near the walls; after this behavior has occurred, there is a reverse trend.

As it was mentioned before, the overall Nusselt number is based on three different heat fluxes; those are the Fourier heat flux due to conduction, the diffusion thermo flux due to Dufour effect and the radiative flux. To demonstrate the contribution of each flux on heat transfer, the distributions of the Fourier, Dufour, and radiative fluxes with τ at $Ra = 10^4$ are shown in Fig. 14. This figure depicts that the greatest effect of optical thickness is for the radiative flux, such that it decreases by increasing τ from surface radiation ($\tau = 0$) up to pure double-diffusion ($\tau >> 1$). This behavior was also reported in a previous study [5]. In contrast, the Dufour and Fourier fluxes have similar combined decreasing and increasing trends with τ and there are local minimum and maximum points in their distributions. Surprisingly, their extreme points take place at equal optical thicknesses, such that the minimum volumes of the Dufour and Fourier fluxes occur at $\tau = 10$ and the maximum values at $\tau = 1000$.

To get a deeper insight into the Dufour, Fourier, and radiation parts of heat transfer, the distributions of three corresponding Nusselt numbers along the y-axis at the left wall of the cavity (the hot surface) are plotted in Fig. 15. This figure shows that the radiative heat transfer is the dominant mechanism and that the maximum value of Nu_{rad} takes place near the bottom wall and the minimum on the top wall. The other two Nusselt numbers are almost uniform, whereas the value of the Fourier Nusselt number is about four times bigger than the Dufour one.

One of the other important parameters in double-diffusive convection is the Sherwood number, which consists of the Fourier and Dufour parts. In Fig. 16, the variations of these two parts along the left wall of the cavity are presented. Based on their definitions, it is expected that they have similar distributions, but different values with the Dufour and Fourier fluxes drawn in the previous figure, as it can be seen from Fig. 15.

In the present analysis, the transient forms of the governing equations are solved, such that the time histories of each dependent variable are also calculated. To demonstrate the transient characteristics of the double-diffusive convection cavity flow, the plots of streamlines, isotherms and iso-concentration lines inside the enclosure at different times are drawn in Figs. 17–19. These figures show how the thermal system spends its transient period up to the steady conditions. Comparing the streamline plots in Fig. 17 to each other shows that the buoyant flow starts from a stagnant position by forming a recirculated zone that occupies the entire space of the cavity, while its center is close to the cold surface. Then, the rate of

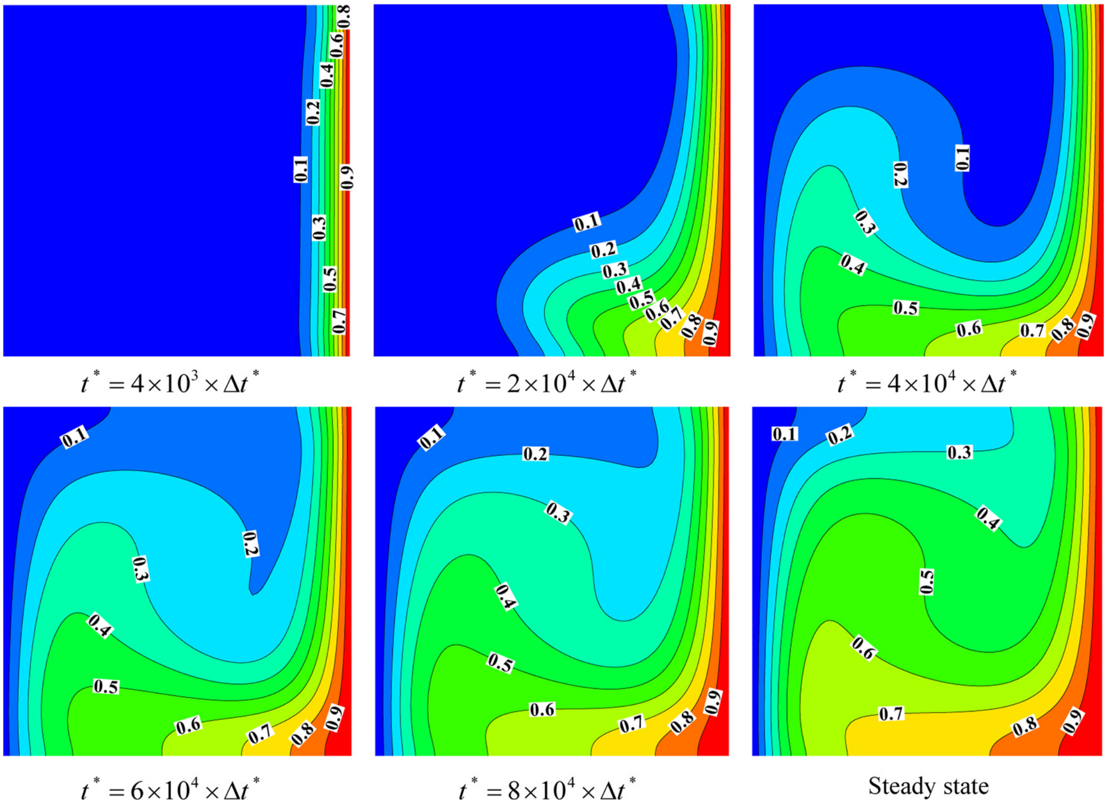
$t^* = 4\times10^3\times\Delta t^*$ $t^* = 2\times10^4\times\Delta t^*$ $t^* = 4\times10^4\times\Delta t^*$

$t^* = 6\times10^4\times\Delta t^*$ $t^* = 8\times10^4\times\Delta t^*$ Steady state

Fig. 19. Iso-concentration lines for $Ra = 10^4$ at different time levels, $\tau = 10$.

vortices increases with time and the center of the recirculated zone shifts towards the cavity center. Besides, a reciprocating trend in the distributions of streamlines with time can be seen from Fig. 17. The temperature distributions inside the cavity at different time levels are depicted in Fig. 18. At the start of heat transfer, the isotherm lines are almost parallel to each other, which shows the dominance of conduction at that time. Then, because of the growing buoyant flow, some curvature appears in the isotherms, such that by increasing in time, the rate of temperature gradient in the horizontal sense decreases near the hot wall and is relaxed, such that, at steady-state conditions, there is almost a uniform temperature gradient inside the cavity from the hot surface toward the cold one. In the case of the concentration field that is shown in Fig. 19, a similar trend, as well as isotherm lines with severe curvature, is observed, although its buoyant force is due to the concentration gradient from the right surface toward the left one. Generally, it can be seen that, for the gas buoyant flow, the temperature and concentration fields spend their transient period from initial values up to the steady-state conditions, such that among these dependent variables the delay of the system to reach the steady-state condition is due to the need of the concentration field for more time for this purpose.

8. Conclusion

In the present work, a double-diffusive convection flow of radiating gas inside a square cavity due to both temperature and concentration gradients is simulated numerically. The set of governing equations, including continuity, vorticity, energy, and mass equations is solved by numerical techniques. The numerical results are presented by plotting streamlines, isotherm, and iso-concentration lines inside the enclosure. Since the gas is considered to be semitransparent, an attempt is made to investigate the effects of optical thickness on the thermal and hydrodynamic behavior of buoyant flow. As a main finding, it should be reminded that, under the presence of a radiating gas in the double-diffusive convection flow, both the velocity and temperature fields of the system are much affected by changes in the value of optical thickness with sweep behavior for these two dependent variables, as optical thickness increases from the non-radiating case ($\tau = 0$) to that of an optically thick medium.

References

[1] P. Kumar, V. Eswaran, A numerical simulation of combined radiation and natural convection in a differential heated cubic cavity, J. Heat Transf. 132 (2009) 023501, http://heattransfer.asmedigitalcollection.asme.org/article.aspx?articleid=1449835.

[2] L.C. Chang, K.T. Yang, J.R. Lloyd, Radiation-natural convection interactions in two-dimensional complex enclosures, J. Heat Transf. 105 (1983) 89–95, http://heattransfer.asmedigitalcollection.asme.org/article.aspx?articleid=1437897.

[3] B.W. Webb, R. Viskanta, Radiation-induced buoyancy-driven flow in rectangular enclosures: experiment and analysis, J. Heat Transf. 109 (1986) 427–433, http://heattransfer.asmedigitalcollection.asme.org/article.aspx?articleid=1439323.

[4] K. Lari, M. Baneshi, S.A. Gandjalikhan Nassab, A. Komiya, S. Maruyama, Combined heat transfer of radiation and natural convection in a square cavity containing participating gases, Int. J. Heat Mass Transf. 54 (2011) 5087–5099, https://doi.org/10.1016/j.ijheatmasstransfer.2011.07.026, http://www.sciencedirect.com/science/article/pii/S0017931011004029.

[5] M. Foruzan Nia, S.A. Gandjalikhan Nassab, A.B. Ansari, Transient combined natural convection and radiation in a double space cavity with conducting walls, Int. J. Therm. Sci. 128 (2018) 94–104, https://doi.org/10.1016/j.ijthermalsci.2018.01.021, http://www.sciencedirect.com/science/article/pii/S1290072917318896.

[6] M.A. Teamah, Numerical simulation of double diffusive natural convection in rectangular enclosure in the presences of magnetic field and heat source, Int. J. Therm. Sci. 47 (2008) 237–248, https://doi.org/10.1016/j.ijthermalsci.2007.02.003, http://www.sciencedirect.com/science/article/pii/S1290072907000634.

[7] Y. Varol, H.F. Oztop, A. Varol, Free convection in porous media filled right-angle triangular enclosures, Int. Commun. Heat Mass Transf. 33 (2006) 1190–1197, https://doi.org/10.1016/j.icheatmasstransfer.2006.08.008, http://www.sciencedirect.com/science/article/pii/S0735193306001588.

[8] M. Rahman, H.F. Öztop, A. Ahsan, M.A. Kalam, Y. Varol, Double-diffusive natural convection in a triangular solar collector, Int. Commun. Heat Mass Transf. 39 (2012) 264–269, https://doi.org/10.1016/j.icheatmasstransfer.2011.11.008, http://www.sciencedirect.com/science/article/pii/S0735193311002521.

[9] F. Moufekkir, M. Moussaoui, A. Mezrhab, M. Bouzidi, N. Laraqi, Study of double-diffusive natural convection and radiation in an inclined cavity using lattice Boltzmann method, Int. J. Therm. Sci. 63 (2013) 65–86, https://doi.org/10.1016/j.ijthermalsci.2012.07.015, http://www.sciencedirect.com/science/article/pii/S1290072912002153.

[10] J. Wang, M. Yang, Y. Zhang, Onset of double-diffusive convection in horizontal cavity with Soret and Dufour effects, Int. J. Heat Mass Transf. 78 (2014) 1023–1031, https://doi.org/10.1016/j.ijheatmasstransfer.2014.07.064, http://www.sciencedirect.com/science/article/pii/S001793101400653X.

[11] M.F. Modest, Radiative Heat Transfer, Academic Press, 2013.

[12] M. Foruzan Nia, S.A. Gandjalikhan Nassab, Conjugate heat transfer study of combined radiation and forced convection turbulent separated flow, Int. J. Nonlinear Sci. Numer. Simul. 18 (2017) 29–39, https://doi.org/10.1515/ijnsns-2015-0134, https://www.degruyter.com/view/j/ijnsns.2017.18.issue-1/ijnsns-2015-0134/ijnsns-2015-0134.xml.

[13] J.H. Ferziger, Numerical Methods for Engineering Application, Wiley, 1981, https://books.google.com/books?id=dp0oAQAAMAAJ.

[14] S.C. Mishra, P. Talukdar, D. Trimis, F. Durst, Two-dimensional transient conduction and radiation heat transfer with temperature dependent thermal conductivity, Int. Commun. Heat Mass Transf. 32 (2005) 305–314, https://doi.org/10.1016/j.icheatmasstransfer.2004.05.015, http://www.sciencedirect.com/science/article/pii/S0735193304001654.

[15] J.D. Hoffman, S. Frankel, Numerical Methods for Engineers and Scientists, CRC Press, 2001, https://www.crcpress.com/Numerical-Methods-for-Engineers-and-Scientists/Hoffman-Hoffman-Frankel/p/book/9780824704438.